Investigation of the correlations between the microstructure and the tensile properties multi-scale composites with a polylactic acid matrix, reinforced with carbon nanotubes and carbon fibers, with the use of the fiber bundle cell theory

L. Mészáros [a,b,*], A. Horváth [a], L.M. Vas [a], R. Petrény [a]

[a] *Department of Polymer Engineering, Faculty of Mechanical Engineering, Budapest University of Technology and Economics, Műegyetem Rkp. 3., H-1111, Budapest, Hungary*
[b] *ELKH-BME Research Group for Composite Science and Technology, Műegyetem Rkp. 3., H-1111, Budapest, Hungary*

A B S T R A C T

In this paper, we established a relationship between the microstructure and the tensile properties of nano- and hybrid composites with a thermoplastic, semi-crystalline poly(lactic acid) (PLA) matrix, reinforced with carbon fibers and carbon nanotubes, using the fiber bundle cell model. The microstructure of the matrix and the volume ratio of the mobile amorphous, rigid amorphous and crystalline fractions were determined by differential scanning calorimetry and the elastic modulus of these fractions was measured by atomic force microscopy. These data served as input parameters for the fiber bundle cell model, in which each structural unit corresponded to a single bundle of fibers. For the parameters for which no experimental method was available, we determined structure-independent constants. With these model parameters, we fitted a fiber bundle cell model curve to the averaged tensile curves of each material. By analyzing the fitted model, we concluded that the mobile and the rigid amorphous fraction of the matrix has a key role in the properties of the initial, load-carrying section of the tensile curve. The crystalline fraction and the carbon nanotubes elongated the failure section. By examining the damage maps, we found that overlapping interphases in the vicinity of carbon fibers and carbon nanotubes improved the load transfer between the carbon fiber and the matrix, thus allowing better utilization of the reinforcing effect of the carbon fibers.

1. Introduction

Polylactic acid (PLA) is one of today's most popular biopolymers. It has the great advantage that it can be produced from feedstocks obtained by fermentation of renewable sources such as corn, cellulose, and also other feedstocks containing polysaccharide. Because of today's environmental consciousness, it can be used on a broader scale in the future, but modifying its strength and chemical properties to meet the requirements of applications is essential. This modification is possible, for example, by producing polymer composites with a PLA matrix [1–3].

Over the last two decades, nanoscale reinforcing materials have become available in addition to the former microscale reinforcing materials. One of the most researched nanoparticles are carbon nanotubes (CNTs) [4,5]. When used as reinforcing material in a thermoplastic polymer matrix, it can not only improve the thermal and electrical conductivity of the polymer composite but it also increases the strength of the composite [6,7]. However, the dispersion of CNTs in matrix

materials is difficult to achieve with mass production technologies (extrusion, injection molding), and aggregates of adhered nanotubes often remain in the matrix. The latter reduces the contact area between the nanotubes and the matrix material, thus reducing their beneficial effects. A solution to this could be reinforcing the matrix with several types of reinforcing materials, thus creating a hybrid composite [8–10]. By adding carbon fibers (CF) to the composite besides the CNTs, the shear stress during the compounding process is then increased by the presence of CF, which helps to disperse the CNTs and so they can exert their reinforcing effect [12,13].

The type and amount of reinforcing materials used and their interaction with each other and the polymer molecules all affect the microstructure of the composite. Former research found that in the case of crystal nucleating reinforcements, a two-layer interphase is formed around them, which has a semi-crystalline inner layer and a rigid amorphous outer layer, and the rest of the matrix is mobile amorphous. If the amount and properties of these phases are taken into account, the

calculation of the mechanical properties of the composite can be much more accurate [14–16].

While the weight fraction of the mobile amorphous (MA), the rigid amorphous (RA), and the crystalline (CR) fractions (F) can be easily measured by differential scanning calorimetry, the measurement of their mechanical properties requires atomic force microscopy (AFM) [17–19]. If the ratio and the mechanical properties of each structural unit, i.e. the CNT, the CF, the MAF, the RAF and the CRF in the composite are known, the mechanical properties of the composite can be calculated.

The correlation between the morphological characteristics, the intrinsic properties of each structural unit and the mechanical properties of the composite, can be easily established with the statistical fiber bundle cell (FBC) model. The FBC model is based on the serial and parallel coupling of elementary fiber bundle cells, corresponding to the structural units of the composite. The stochastic mechanical properties of the fiber bundle cells make the model suitable for describing the response to external mechanical stress and the failure of each structural unit and also of the whole composite, which is also a stochastic process [20–23].

This study focuses on the microstructure of nano- and hybrid composites, with particular emphasis on the structural and mechanical behavior of the interphase around the reinforcing material. Using the results of differential scanning calorimetry (DSC) and atomic force microscopy (AFM), we aimed to construct a fiber bundle cell model, which establishes a link between the microstructure of the material, the intrinsic properties of the microstructural units and the tensile test results.

2. Materials and methods

2.1. Materials

We used PLA matrix and nanocomposites containing carbon nanotubes in four different weight ratios to investigate the effect of carbon nanotubes on the morphology and mechanical properties. We also prepared composites containing only carbon fibers, and carbon fibers and four different amounts of carbon nanotubes to study the combined effect of nanotubes and microfibers. The composition of the materials is shown in Table 1.

The matrix material used for nano- and hybrid composites was Ingeo 4043D (NatureWorks LLC, USA) polylactic acid. It has a tensile strength of 53 MPa, a tensile modulus of 3.6 MPa, and an elongation at break of 6%. Its density was 1.24 g/cm^3, and its melt flow index (MFI) (2.16 kg/ 210 °C) was 6 g/10 min. It had a D-lactide content of 4.8%, which makes it capable of crystallizing.

The Nanocyl NC7000 (Nanocyl SA, Belgium) multi-walled carbon nanotubes were produced by catalytic chemical vapor deposition. They had an average diameter of 9.5 nm, an average length of 1.5 μm, a carbon content of 90 wt%, and less than 1 wt% of transition metal oxides. Their specific surface area varied between 250 and 300 m^2/g.

The PANEX PX35 (Zoltek Zrt., Hungary) chopped carbon fibers had a tensile strength of 3800 MPa, a tensile modulus of 242 GPa and an elongation at break of 1.5%. They had a density of 1.81 g/cm^3, a fiber diameter of approximately 7.2 μm, and a carbon content of 95%. The initial fiber length was 6 mm, and the fibers had silane sizing.

2.2. Production of the samples

Before compounding, the PLA was dried in a Faithful WGLL-125 BE (Huanghua Faithful Instrument Co., LTD, China) drying oven for 4 h at 80 °C. First, the reinforcing materials were mechanically mixed with the PLA granules, then the materials were compounded with a Labtech Engineering Co., Ltd. LTE 26-44 twin-screw extruder (Labtech Engineering Co., Ltd., Thailand) with a screw speed of 25 1/min and zone temperatures of 180, 190, 190, 190, 190, 200, 200, 200, 200 and 200 °C and die temperature of 190 °C. Granules with an approximate length of

Table 1
Composition of the materials.

CNT [weight%]	0	0.25	0.5	0.75	1.00	0	0.25	0.5	0.75	1.00
CF [weight%]	0	0	0	0	0	30	30	30	30	30
Materials:	PLA	PLA+0.25 CNT	PLA+0.5 CNT	PLA+0.75 CNT	PLA+1CNT	PLA+30CF	PLA+30CF+0.25CNT	PLA+30CF+0.5 CNT	PLA+30CF+0.75CNT	PLA+30CF+1CNT

4 mm were prepared from the filaments produced during compounding with a Labtech LZ-120/VS (Labtech Engineering Co., Ltd., Thailand) granulator. Before injection molding, the granules were dried again at 80 °C for 4 h.

According to EN ISO 527-2:2019, 1A type dumbbell tensile specimens were produced by an Arburg Allrounder Advance 270S 400-170 (Arburg GmbH, Germany) injection molding machine, with a melt temperature of 200 °C, a mold temperature of 25 °C and an injection pressure of 1200 bar. During the injection molding of the specimens, the high cooling rate left the matrix in an amorphous state (APLA), therefore the PLA had to be crystallized by annealing for the preparation of semi-crystalline polylactic-acid matrix (PCPLA) composites. The samples were annealed at 100 °C for 1 h in a Faithful WGLL-125 BE oven [24] between two press plates to minimize shrinkage.

2.3. Structural and mechanical characterization of the samples

To determine the phase structure of the PCPLA matrix material, we measured the mobile amorphous (MAF), the rigid amorphous (RAF) and the crystalline fraction (CRF) by modulated differential scanning calorimetry (MDSC) using a TA Instruments Q2000 (TA Instruments, USA) differential scanning calorimeter. The temperature range of the test was 0–200 °C, and the heating rate was 5 °C/min. The amplitude of modulation was 1 °C, with a period of 60 s. The test was performed in a nitrogen atmosphere with a flow rate of 50 ml/min. The weight of the samples was 10–15 mg. The weight ratio of the mobile amorphous fraction can be calculated by equation (1) [25]:

$$MAF(\%) = \frac{\Delta c_p}{\Delta c_{p0}} \bullet 100 \ (\%) \tag{1}$$

where Δc_p is the measured heat capacity jump at the glass transition temperature (T_g) and $\Delta c_{p0} = 0,48 \frac{J}{g}$ is the heat capacity jump at T_g of the 100% amorphous PLA. The latter was measured on a fully amorphous PLA sample. The weight ratio of the crystalline fraction (CRF) can be calculated according to equation (2) [25]:

$$CRF(\%) = \frac{\Delta H_m}{\Delta H_0 \left(1 - \varphi_{f,wt}\right)} \cdot 100 \ (\%) \tag{2}$$

where ΔH_m is the measured crystal melting enthalpy, $\Delta H_0 = 93 \frac{J}{g}$ is the crystal melting enthalpy of the 100% crystalline PLA [26], and $\varphi_{f,wt}$ is the weight ratio of the reinforcement. The ratio of the rigid amorphous fraction can be calculated according to equation (3)

$$RAF(\%) = 100\% - MAF(\%) - CRF(\%) \tag{3}$$

The modulus of the mobile amorphous, rigid amorphous, and the crystalline phases in the matrix was determined by atomic force microscopy (force and displacement were measured) with a Nanosurf

FlexAFM 5 (Nanosurf AG, Switzerland) atomic force microscope with a BudgetSensors Tap 190 Al-G tip (Innovative Solutions Bulgaria Ltd., Bulgaria). To make the structural units measurable, the surfaces of the samples were etched in a 5 mol/l NaOH solution for 1 h at 25 °C [27]. First, images were made of a spherulite in the pure PCPLA matrix, of a carbon fiber and its vicinity in a composite with an APLA matrix reinforced with only carbon fiber, and of a pure APLA matrix. Then force–indentation measurements were made with an indentation depth of 2 μm and an indentation time of 33 ms. The moduli were calculated with the ANA software (Nanosurf AG, Switzerland) with the use of the Derjaguin-Muller-Toporov model [28]. The modulus of the CRF was measured along a straight line passing through a spherulite; for RAF it was near a carbon fiber in an amorphous PLA matrix, and for MAF it was determined on a randomly chosen part on the unreinforced, amorphous matrix. 20 points were measured and averaged in each case, with a straight line fitted for all three phases. In Fig. 1, the red lines indicate the lines along which the measurement points were located.

The measured moduli of the different phases in the matrix are shown in Table 2. The large standard deviation of the results is presumably caused by the uncertainty of the measurement location, because the AFM tip is very small (~1 nm) and due to its small surface area in contact with the sample, the mechanical properties vary greatly depending on the location, especially for the interphases.

The post-crystallized PLA (PCPLA) matrix composites were tested with a Zwick Z20 (ZwickRoell GmbH & Co. KG, Germany) tensile tester, and the stress–strain curves were recorded. Before the tests, the samples were conditioned in a desiccator at 50% RH for 4 weeks. Five samples of each material were measured with a tensile speed of 2 mm/min and the resulting stress-specific strain curves of the same materials were averaged at each point.

2.4. Modeling the relationship between structural and mechanical properties

If the tensile stress is recorded up to ultimate failure during a tensile test of a homogeneous material (consisting of a single bundle of fibers), and the tensile curves obtained from repeated tests are averaged point by point, the resulting tensile curve can be divided into two parts: the first is the load-carrying or deformation section, the second is the failure

Table 2
Moduli of the different phases in the matrix.

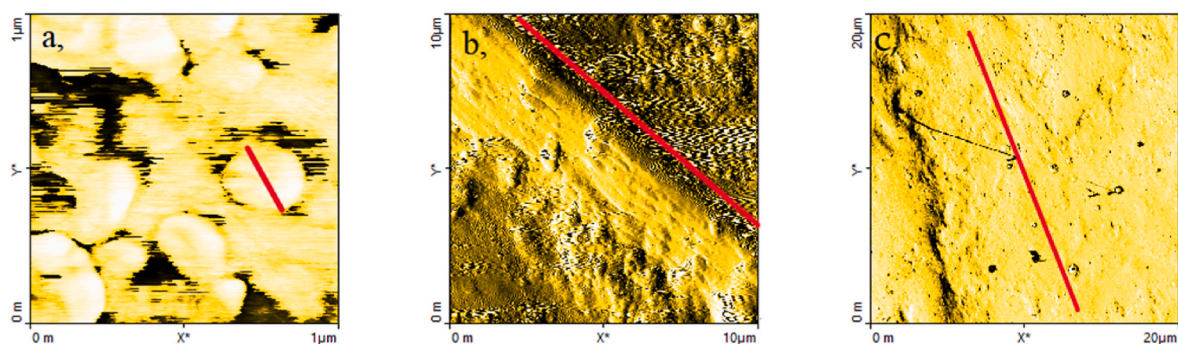|	Modulus of the crystalline phase (GPa)	Modulus of the rigid amorphous phase (GPa)	Modulus of the mobile amorphous phase (GPa)
Average	3.140	2.557	1.603
Standard deviation	1.864	1.680	0.452

Fig. 1. Atomic force microscopy images of the nano- and the hybrid composites, and the location of the force–displacement measurements. a) crystalline phase in a spherulite, b) rigid amorphous phase around a carbon fiber in the amorphous PLA matrix, composite reinforced with only CF, c) mobile amorphous phase in the pure amorphous PLA.

section (Fig. 2 a).

The initial section of such a tensile curve can be approximated with a characteristic tensile function, and the failure section can be taken into account with a reliability function since failure is a stochastic process. The model curve describing the full curve can be obtained as the product of the two functions (Fig. 2 b) [23]. In a composite material, the micro- and nanoscale reinforcing fibers, and even the molecule chains of the polymer matrix, can be considered fibrous structures. The fibers of these structures that have the same characteristics are called fiber bundle cells. Considering a single fiber bundle cell with viscoelastic behavior, the load carrier section of its tensile curve can be modeled as the response of the Standard-solid model to a velocity jump excitation (4) [20]:

$$\sigma(\varepsilon) = a\left(1 - e^{-b\varepsilon}\right) + c\varepsilon \tag{4}$$

where $\sigma(\varepsilon)$ is the characteristic tensile function, ε is the specific elongation, a is a stress, c is a modulus-type constant and b is an elongation constant. The failure section of the curve can be described with a responsibility function ($R(\varepsilon)$), which is a complementary Gaussian-distribution function in a general case (5) [20]:

$$R\left(\varepsilon, M, D, D^2\right) = 1 - Q(\varepsilon, M, D) = 1 - \int_{-\infty}^{\varepsilon} \frac{1}{D\sqrt{2\pi}} \cdot e^{\frac{(t-M)^2}{2D^2}} \mathrm{d}t \tag{5}$$

where the parameter M is the mean of the distribution, and the parameter D is its standard deviation. The variance of the distribution is D^2. The condition for applying a normal distribution is that $M - 3D > 0$, to avoid the elongation being negative. Therefore, the function describing the total measured tensile curve ($\sigma_{measured}(\varepsilon)$, equation (6)) can be obtained as the product of the functions describing the load-carrying (equation (4)) and the failure section of the curve (equation (5)) [20]:

$$\sigma_{measured}(\varepsilon) \approx \sigma_{model}(\varepsilon) = \sigma(\varepsilon) \bullet R(\varepsilon, M, D) \tag{6}$$

Composites are structures built up of several different fibrous parts, so to describe their full tensile curve, a weighted parallel coupling of several elementary fiber bundle cells is required. Then the measured tensile curve of a composite material can be modeled as follows (7) [20]:

$$\sigma_{measured}(\varepsilon) \approx \sigma_{model}(\varepsilon) = \sum_{i=1}^{n} p_i \sigma_i(\varepsilon) R_i(\varepsilon, M_i, D_i) =$$

$$= \sum_{i=1}^{n} p_i \left(a_i\left(1 - e^{-b_i\varepsilon}\right) + c_i\varepsilon\right) \left(1 - \int_{-\infty}^{\varepsilon} \frac{1}{D_i\sqrt{2\pi}} \cdot e^{-\frac{(t-M_i)^2}{2D_i^2}} \mathrm{d}t\right) \tag{7}$$

where p_i is the weight ($\sum_{i=1}^{n} p_i = 1$), $\sigma_i(\varepsilon)$ is the characteristic tensile function and $R_i(\varepsilon)$ is the reliability funcion of the i-th fiber bundle cell, and n is the number of fiber bundle cells coupled in parallel. The goodness of fit of the model curve to the measured curve can be shown with the relative mean squared error (RMSE, equation (8)) [20]:

$$RMSE = \frac{\sqrt{\frac{1}{N}\sum_{j=1}^{N}\left(\sigma_{measured}\left(\varepsilon_j\right) - \sigma_{model}\left(\varepsilon_j\right)\right)^2}}{\max\limits_{1 \le j \le N}\sigma_{measured}\left(\varepsilon_j\right)} \tag{8}$$
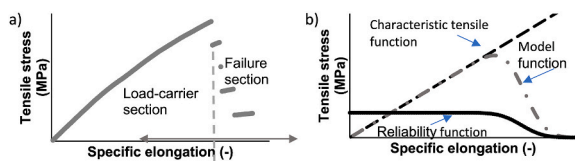

Fig. 2. a) separating the tensile curve into a load-carrier and a failure section, b) generating of the model function from a characteristic tensile function and a reliability function.

where N is the number of the measured data points. Equation (9) gives a quotient, which is the stress response of k fiber bundle cells compared to the force response of a model of n fiber bundle cells. This equation gives a stress quotient map as a function of specific elongation using stress lines $k = 1, …, n$. This map shows the role of each cell in load absorption [20].

$$P_{k,model}(\varepsilon) = \frac{\sum_{i=1}^{k} p_i \sigma_i(\varepsilon) R_i(\varepsilon)}{\sum_{i=1}^{n} p_i \sigma_i(\varepsilon) R_i(\varepsilon)} \tag{9}$$

where $P_{k,model}(\varepsilon)$ is the tensile stress component as a function of specific elongation, $P_{n,model}(\varepsilon) = 1$ for every ε, and $1 \le k \le n$ is the number of a given fiber bundle cell. The resultant curves create a kind of failure map where the ranges between the curves characterize the participation of the components and the failure processes represented by them.

3. Results and discussion

3.1. Microstructure of the nano- and hybrid composites

Based on the DSC tests, 3 phases can be differentiated in the matrix of the PCPLA matrix composites: crystalline, rigid amorphous, and mobile amorphous. Fig. 3 a shows that the proportion of the crystalline fraction is smaller, while the rigid amorphous fraction is larger in the nano-composites than in the pure PLA. Beyond this, no clear trends can be observed because the random volume distribution of nanotubes and their aggregates means that the proportion of phases formed in the matrix is also random. In the only carbon fiber–reinforced PCPLA composite, the crystalline fraction decreased, while the volume fraction of the rigid amorphous phase increased significantly compared to pure PCPLA (Fig. 3 b). It can be assumed that they act as crystal nucleating agents, and the average crystallite size is then significantly reduced. The carbon nanotubes caused a slight decrease in the crystalline fraction but a significant increase in the proportion of the rigid amorphous phase, indicating that the average crystallite size decreased. This suggests that the nanotubes acted as crystal nucleating agents and that the better dispersion of the nanotubes caused simultaneous crystallization in many more sites of the matrix material, resulting in a smaller crystallite size [29].

3.2. Mechanical properties of the nano- and hybrid composites

The tensile strength, the tensile modulus and the elongation at break of the only carbon nanotube reinforced composites did not change significantly compared to the pure PLA (Table 3). However, in the carbon fiber reinforced composites, the addition of the carbon nanotubes increased the tensile strength and modulus significantly, and a slight increase is observable also in the strain at break values. This indicates that the carbon nanotubes improved load transfer between the matrix and the carbon fibers. To further investigate this, we fitted a fiber bundle cell model to the measured tensile curves.

3.3. Mechanical properties of the structural units in the matrix

Based on the DSC tests, and the weight fraction of the reinforcing materials, the p_i weight for each bundle was the volume fraction of the structural units relative to the total composite volume. For this, the weight fractions from the DSC test for CRF, RAF and MAF and the weight fraction of the added reinforcing materials were converted to volume ratios using the densities of the different phases. The parameter c_i in equation (7) is the initial tangent tensile modulus; for CNT and CF, it was calculated from their elastic modulus (E). It is important to note that the orientation of CNT and CF in each bundle is not considered parallel to the direction of loading. Hence, their elastic modulus values need to be
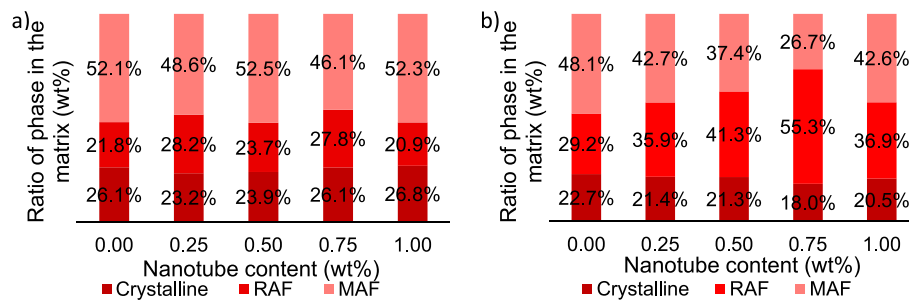
Fig. 3. The ratio of mobile amorphous, rigid amorphous, and crystalline phases a) in the pure PCPLA, and in the PCPLA matrix nanocomposites b) in the carbon fiber–reinforced PCPLA, and in the hybrid composites with a PCPLA matrix.

Table 3
Mechanical properties of the nano-and hybrid composites.

	Tensile strength (MPa)			Elongation at break (%)			Modulus (MPa)		
PLA	64.4	±	0.6	3.2%	±	0.3%	3217.4	±	45.7
PLA+0.25CNT	64.0	±	0.8	3.3%	±	0.5%	3211.8	±	79.0
PLA+0.5CNT	64.4	±	0.6	3.7%	±	0.3%	3259.8	±	12.5
PLA+0.75CNT	65.4	±	0.7	3.1%	±	0.5%	3314.2	±	49.6
PLA+1CNT	65.0	±	0.5	2.9%	±	0.2%	3266.4	±	70.8
PLA+30CF	62.3	±	1.9	1.4%	±	0.1%	7235.8	±	220.4
PLA+30CF +0.25CNT	100.0	±	5.9	1.4%	±	0.1%	7521.8	±	308.8
PLA+30CF +0.5CNT	107.4	±	2.1	1.6%	±	0.1%	7277.3	±	445.1
PLA+30CF +0.75CNT	102.0	±	3.2	1.4%	±	0.1%	7606.8	±	565.4
PLA+30CF +1CNT	98.6	±	2.7	1.4%	±	0.1%	7622.1	±	471.7

corrected (E_{corr}) with an efficiency factor f.

$$E_{corr} = f \bullet E \qquad (10)$$

If the fibers are randomly oriented in three dimensions, the value of f is 0.2 [30]. Based on the tensile modulus from the CNT and CF data-sheets, the corrected tensile modulus (E_{corr}) was calculated, which provided the parameter c_i for these phases (Table 4). For the bundles representing MAF, RAF, and CRF, which constitute the matrix material, atomic force microscopy gave the value of parameter c. For the mobile amorphous, the rigid amorphous, and the crystalline phase, the average of the modulus values measured at each point, expressed in MPa (E_i), provided the parameter c_i for a given bundle in the model. For the model described by equation (7), parameters a_i and b_i were determined. Our goal was to fit the model as accurately as possible to the point-averaged tensile curves that we obtained by evaluating the tensile tests. These parameters were determined to be constant, independently of the reinforcing material content. As the initial modulus of the cumulative model curve had to be non-negative, the values of the parameters had to be chosen to satisfy equation (11). All the parameters for each model can be found in Tables S1 and S2 in the supplementary file.

$$E_0 = a_i \bullet b_i + c_i \geq 0 \qquad (11)$$

Table 4
Example of the model parameters for the PCPLA+30CF+1CNT composite.

	Measured	Fitted and kept constant for each material		Measured or calculated	Calculated (for control)	Fitted for each material	
Bundle	p_i (-)	a_i (MPa)	b_i (-)	c_i (MPa)	E_0 (MPa)	$M_i(\varepsilon)$ (-)	$D_i(\varepsilon)$ (-)
MAF	0.3314	6600	0.5	1600	4900	0.003636	0.001818
RAF	0.2860	-7000	0.1	2557	1857	0.001818	0.002727
CRF	0.143	-5500	0.3	3140	1490	0.016364	0.001818
CNT	0.00757	-270000	0.5	211000	560	0.013636	0.004545
CF	0.232	0	0	35000	35000	0.012818	0.000909

3.4. Structure–mechanical properties relationships in the composites

We used four bundles for the samples not containing CNTs and five for all other nano- and hybrid composites. These bundles represented the mobile amorphous (MAF), rigid amorphous (RAF), crystalline (CRF), CNT, and CF phases of the materials, corresponding to their structure. The unreinforced PLA matrix material is composed of a CRF, a RAF, and a MAF. We divided the latter into two bundles. The initial section and the peak of the tensile curve were defined by a bundle of breaking fibers (breaking MAF), which were used to describe the breakage of the molecular chains. The plateau-like section following the force peak was followed by a 0 c parameter bundle (sliding MAF), which represented the sliding molecular chains. In the case of nanocomposites containing CNTs, a bundle (CNT) characterizing the behavior of nanotubes was also used in addition.

Since the initial slope of the curves is given (measured), their expected elongation at break values (M_i) and the standard deviation (D_i) have been chosen to fit as closely as possible to the failure steps of the measured curves. According to this, the earliest failure occurs in the rigid amorphous phase, followed by the breaking molecular chains forming the mobile amorphous phase and then the sliding fibers. Then the CNTs break, and final failure occurs in the crystalline phase. The curve fits (Fig. 4) for the unreinforced PLA matrix and the nanocomposites indicate that the load absorption and tensile strength of the specimens were mainly determined by RAF and breaking MAF, and CNT and CRF determined failure. The effect of the rigid amorphous phase affects the initial phase of the curves, as the initial slope of the curve is greater, especially for higher nanotube contents, after which the curve breaks slightly and decreases in slope. It is because the stiffness of RAF and MAF differs greatly, so the interphase between them slips. The sliding MAF initially has a significant effect on both the load absorption and the failure of the specimens and then becomes less involved as CNT content increases. While in the case of unreinforced PLA, CRF mainly affects only the progress of failure, the effect on the tensile strength of the samples with CNT is also significant; this is particularly evident in the case of the curve fitting of the PCPLA0.5CNT sample. Consequently,
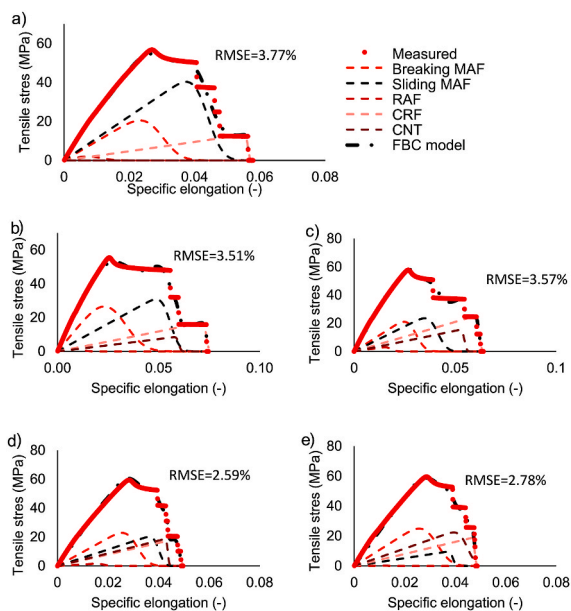
Fig. 4. Fitting of the fiber bundle cell model on the pure PCPLA and the PCPLA matrix nanocomposites a) PCPLA, b) PCPLA+0.25CNT, c) PCPLA+0.5CNT, d) PCPLA+0.75CNT e) PCPLA+1CNT.

in addition to destruction, the upslope and plateau phases of the curves are also increasingly affected by CNTs.

On the failure maps (Fig. 5), the ranges between the curves characterize the participation of the components and the failure processes represented by them. For the pure PCPLA and CNT, the breaking and the sliding mobile amorphous fraction govern the initial section of load uptake, and the rigid amorphous fraction has a significant effect on it.
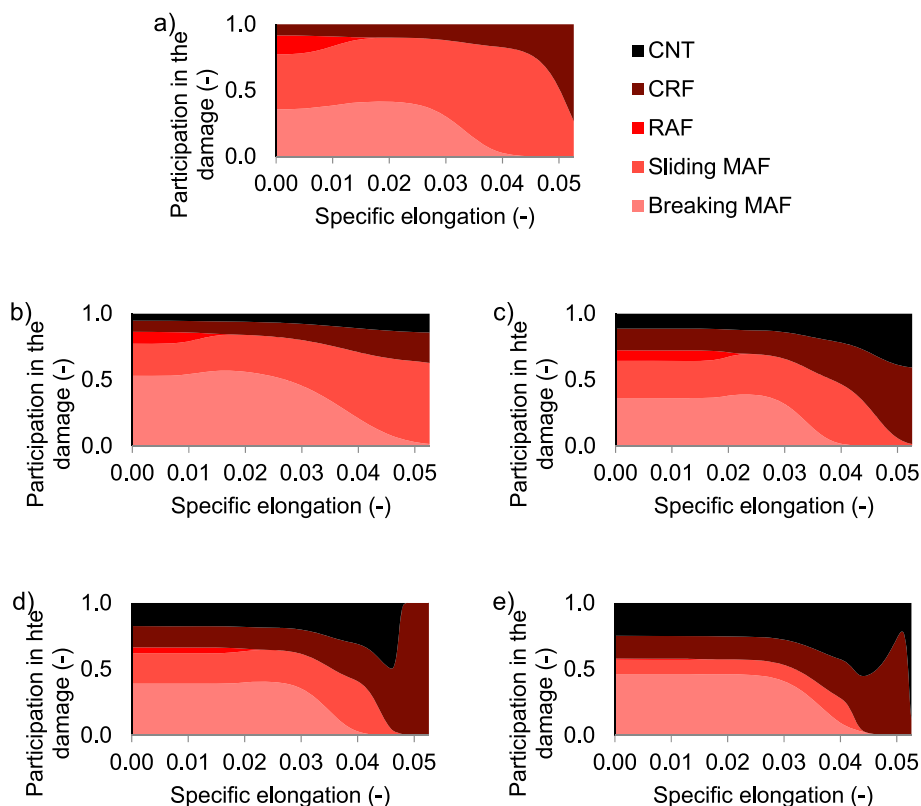
The crystalline fraction plays an important role in the damage section, inhibiting crack propagation. The role of the rigid and mobile amorphous fractions in the nanocomposites are similar, but their effect is more elongated. In the nanocomposites, the carbon nanotubes and the crystalline fraction govern the damage, as both can slow crack propagation.

When modeling the hybrid composites, we used the bundles already described for nanocomposites, with some modifications (Fig. 6). Since the failure of the fiber-reinforced materials occurred after a much lower elongation than for the nanocomposites, no sliding molecular parts were formed, and the sliding MAF bundle was therefore omitted. In addition, the presence of the CF reinforcing material necessitates the use of another bundle.

Accordingly, the sample reinforced with carbon fibers only was modeled with four bundles, and all other hybrid composites with five bundles, where each bundle represents the mobile amorphous (MAF), rigid amorphous (RAF), crystalline (CRF), CNT, and CF phases of the material. Based on the fitted expected elongation at break $M_i(\varepsilon)$, we assume that in this case, too, the rigid amorphous phase is the first to initiate failure by sliding, followed by the breaking of the molecular chains of the mobile amorphous phase. It is followed by the breaking of the carbon fibers, then the nanotubes, and finally, failure in the crystalline phase.

The damage maps of the carbon fiber–reinforced composites (Fig. 7) show that the damage is mainly governed by the carbon fibers. However, as carbon nanotube content is increased, the participation of the mobile and rigid amorphous and the crystalline fraction, and also the carbon nanotubes becomes more significant. It can be explained with the fact that overlapping interphases in the vicinity of the carbon fibres and carbon nanotubes provide a more efficient load transfer between the matrix and the reinforcing material, thus allowing a better utilization of the reinforcing effect of the carbon fibers.

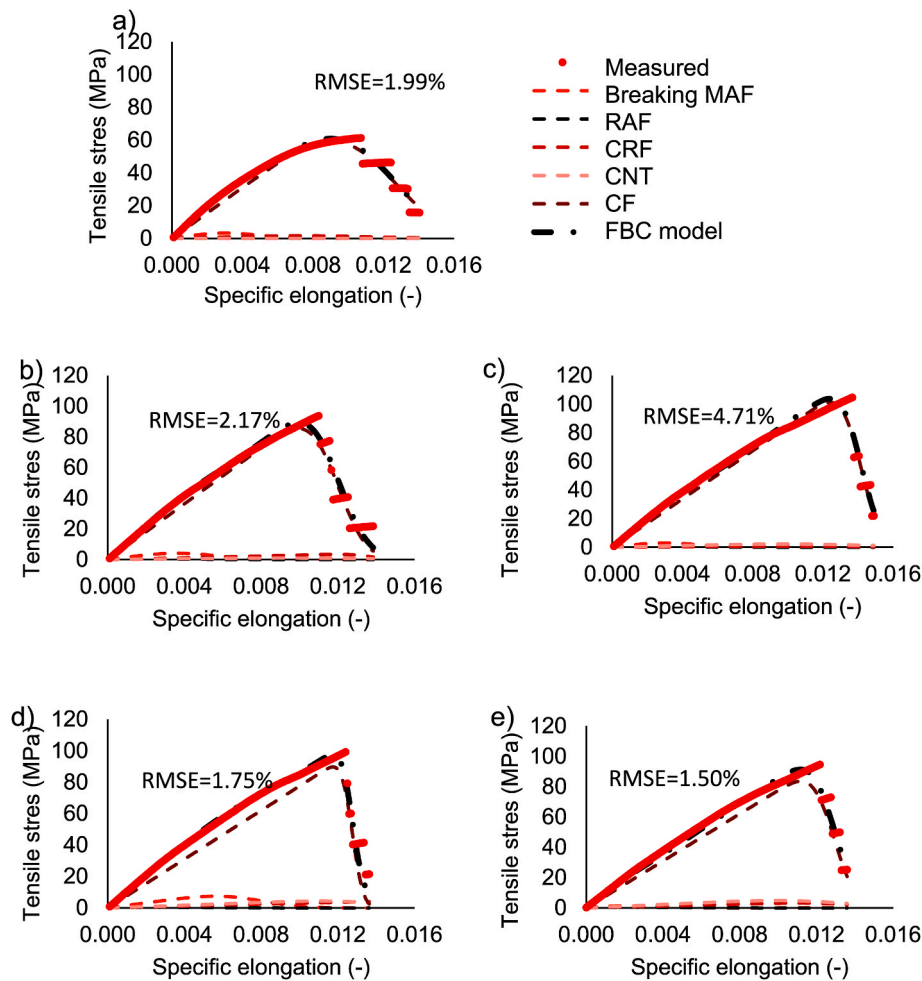The role of the structural units in the tensile properties can be better

Fig. 5. Failure maps of the pure PCPLA and of the PCPLA matrix nanocomposites a) PCPLA, b) PCPLA+0.25CNT, c) PCPLA+0.5CNT, d) PCPLA+0.75CNT e) PCPLA+1CNT.

Fig. 6. Fitting of the fiber bundle cell model on the carbon fiber–reinforced PCPLA, and the PCPLA matrix hybrid composites, a) PCPLA+30CF, b) PCPLA+30CF +0.25CNT, c) PCPLA+30CF +0.5CNT, d) PCPLA+30CF +0.75CNT e) PCPLA+30CF +1CNT.

analyzed if their expected elongation at break values ($M_i(\varepsilon)$) are plotted as a function of CNT content (Fig. 8). The expected elongation at break of the bundle corresponding to the sliding MAF increases with 0.25 wt% CNT compared to the unreinforced PLA matrix material and then decreases with increasing CNT content. It is because, for low nanotube content, only a small amount and small aggregates were present in a given cross-section, and therefore the sliding of the MAF was easier as nothing hindered it. The $M_i(\varepsilon)$ value of the bundle, associated with the CRF also increased at 0.25 wt% CNT content and then started to decrease significantly. It can be explained by the fact that in the case of uniformly distributed CNTs, the distribution of CRF around the nanotubes is also uniform, thus contributing effectively to load carrying. The expected elongation at break of the bundle representing CNT increases up to 0.50 mass fraction of CNT content, above which it starts to decrease, which also can be explained by the larger aggregate size.

In the fiber reinforced composites, the $M_{RAF}(\varepsilon)$ parameter of the bundle belonging to the RAF remained almost independent of CNT content, whereas the parameters of the other bundles showed significant increment. The expected elongation at break of the CRF increased monotonically with CNT content, presumably due to the dispersing effect of the carbon fiber. If the carbon nanotubes and the crystalline parts (grown on the nanotubes), and the rigid amorphous interphase associated with them are dispersed uniformly, the breakage of the mobile amorphous parts does not lead to a full cross-sectional damage, thus the ultimate failure of the specimen occurs at higher specific elongation.

4. Conclusions

In this study, we established a relationship between the microstructure and the tensile properties of nano- and hybrid composites with a thermoplastic, semi-crystalline PLA matrix, reinforced with carbon fibers and carbon nanotubes, using the fiber bundle cell model. First, the microstructure of the nano-and hybrid composites and the volume ratio of each structural unit were determined by differential scanning calorimetry. Then we measured the elastic modulus of each structural unit by atomic force microscopy. These data served as input parameters for the fiber bundle cell model, in which each structural unit corresponded to a single fiber bundle. For the parameters for which no experimental method was available, we determined the most accurate model fit feasible, so that they were, as far as possible, structure-independent constants for the bundle. With these model parameters, we fitted a model curve to the averaged tensile curves of each material. By analyzing the fitted model, we concluded that the mobile and the rigid amorphous fraction of the matrix had a key role in the properties of the initial, load-carrying section of the tensile curve, while the crystalline fraction and the carbon nanotubes elongated the failure section. The damage maps indicated that overlapping interphases in the vicinity of reinforcing materials of different scales improved the load transfer between the carbon fiber and the matrix, thus allowing better utilization of the reinforcing effect of the carbon fibers.
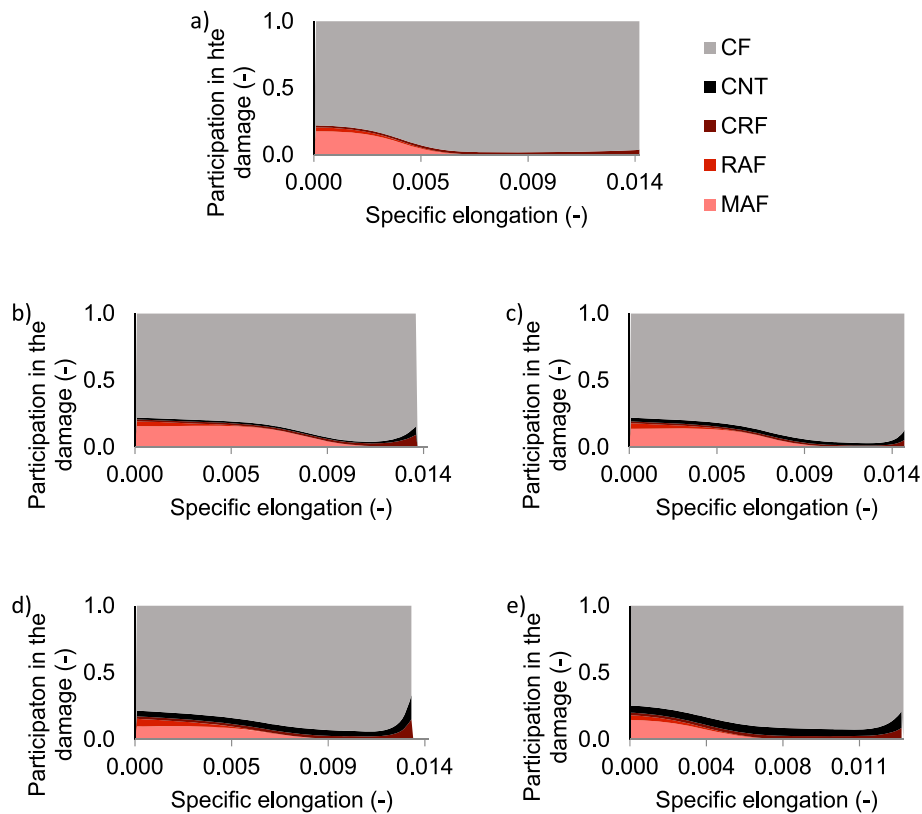
Fig. 7. Failure maps of the carbon fiber–reinforced PCPLA and of the PCPLA matrix hybrid composites a) PCPLA+30CF, b) PCPLA+30CF +0.25CNT, c) PCPLA+30CF +0.5CNT, d) PCPLA+30CF +0.75CNT e) PCPLA+30CF +1CNT.
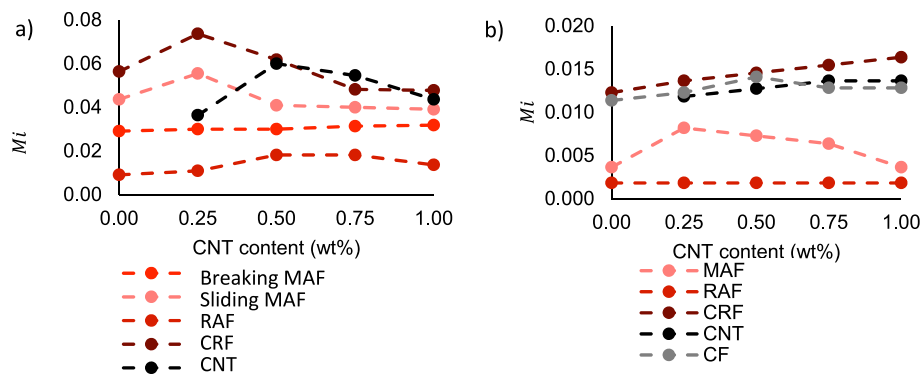

Fig. 8. Expected elongation at break values as a function of the carbon nanotube content of a) the pure PCPLA, and of the PCPLA matrix nanocomposites, b) the carbon fiber reinforced and the hybrid composites.

Author contribution statement

László Mészáros: supervision, reviewing the manuscript, results evaluation.

Aurél Horváth: results evaluation, experimental work.

László Mihály Vas: experimental design, reviewing the manuscript.

Roland Petrény: manuscript writing, results evaluation, experimental work.

Declaration of competing interest

The authors declare that they have no known competing financial interests or personal relationships that could have appeared to influence the work reported in this paper.

Data availability

No data was used for the research described in the article.

Acknowledgements

Appendix A. Supplementary data

Supplementary data to this article can be found online at https://doi.org/10.1016/j.compscitech.2023.110154.

References

[1] C. Vigneswaran, M. Ananthasubramanian, P. Kandhavadivu, in: C. Vigneswaran, M. Ananthasubramanian, P.B.T.-B. of T. Kandhavadivu (Eds.), 8 - Biotechnology and Biomaterials for Hygienic and Health Care Textiles, Woodhead Publishing India, 2014, pp. 398–433, https://doi.org/10.1016/B978-93-80308-42-5.50008-1.

[2] Q. Qin, Y. Yang, C. Yang, L. Zhang, H. Yin, F. Yu, J. Ma, Degradation and adsorption behavior of biodegradable plastic PLA under conventional weathering conditions, Sci. Total Environ. 842 (2022), 156775, https://doi.org/10.1016/j.scitotenv.2022.156775.

[3] G. Zhao, H.-Y. Liu, X. Cui, X. Du, H. Zhou, Y.-W. Mai, Y.-Y. Jia, W. Yan, Tensile properties of 3D-printed CNT-SGF reinforced PLA composites, Compos. Sci. Technol. 230 (2022), 109333, https://doi.org/10.1016/j.compscitech.2022.109333.

[4] S.S. Zamir, B. Fathi, A. Ajji, M. Robert, S. Elkoun, Phase transition and crystallization behavior of grafted starch nanocrystals in PLA nanocomposites, Express Polym. Lett. 16 (2022) 1253–1266, https://doi.org/10.3144/expresspolymlett.2022.91.

[5] B. Wang, Q. Zheng, M. Li, S. Wang, S. Xiao, X. Li, H. Liu, Enhancing interfacial interactions of cocontinuous poly(lactic acid)/polyethylene blends using vinylsilane grafted carbon nanotubes as generic reactive compatibilizers, Express Polym. Lett. 16 (2022), https://doi.org/10.3144/expresspolymlett.2022.39.

[6] S.S. Ray, Electrical and thermal conductivity of environmentally friendly polymer nanocomposites (EFPNCs) using biodegradable polymer matrices and clay/carbon nanotube (CNT) reinforcements, in: S.S. Ray (Ed.), Friendly Polymer Nanocomposites, Woodhead Publishing, 2013, pp. 450–464, https://doi.org/10.1533/9780857097828.2.450.

[7] R. Petrény, C. Tóth, A. Horváth, L. Mészáros, Development of electrically conductive hybrid composites with a poly(lactic acid) matrix, with enhanced toughness for injection molding, and material extrusion-based additive manufacturing, Heliyon 8 (2022), e10287, https://doi.org/10.1016/j.heliyon.2022.e10287.

[8] M.K. Hassanzadeh-Aghdam, M.J. Mahmoodi, R. Ansari, Creep performance of CNT polymer nanocomposites -An emphasis on viscoelastic interphase and CNT agglomeration, Compos. B Eng. 168 (2019) 274–281, https://doi.org/10.1016/j.compositesb.2018.12.093.

[9] H. Du, C. Fang, J. Zhang, X. Xia, G.J. Weng, Segregated carbon nanotube networks in CNT-polymer nanocomposites for higher electrical conductivity and dielectric permittivity, and lower percolation threshold, Int. J. Eng. Sci. 173 (2022), 103650, https://doi.org/10.1016/j.ijengsci.2022.103650.

[10] A.H. Esbati, S. Irani, Effect of functionalized process and CNTs aggregation on fracture mechanism and mechanical properties of polymer nanocomposite, Mech. Mater. 118 (2018) 106–119, https://doi.org/10.1016/j.mechmat.2018.01.001.

[12] K. Skórczewska, K. Lewandowski, S. Wilczewski, Novel composites of poly(vinyl chloride) with carbon fibre/carbon nanotube hybrid filler, Materials 15 (2022), https://doi.org/10.3390/ma15165625.

[13] M.R. Zakaria, H. Md Akil, M.H. Abdul Kudus, F. Ullah, F. Javed, N. Nosbi, Hybrid carbon fiber-carbon nanotubes reinforced polymer composites: a review, Compos. B Eng. 176 (2019) 107313, https://doi.org/10.1016/j.compositesb.2019.107313.

[14] M. Ries, F. Weber, G. Possart, P. Steinmann, S. Pfaller, A quantitative interphase model for polymer nanocomposites: verification, validation, and consequences regarding size effects, Composer Part A Appl. Sci. Manuf. 161 (2022), 107094, https://doi.org/10.1016/j.compositesa.2022.107094.

[15] R. Petrény, L. Almásy, L. Mészáros, Investigation of the interphase structure in polyamide 6–matrix, multi-scale composites, Compos. Sci. Technol. 225 (2022), 109489, https://doi.org/10.1016/j.compscitech.2022.109489.

[16] B. Zhu, Y. Wang, H. Liu, J. Ying, C. Liu, C. Shen, Effects of interface interaction and microphase dispersion on the mechanical properties of PCL/PLA/MMT nanocomposites visualized by nanomechanical mapping, Compos. Sci. Technol. 190 (2020), 108048, https://doi.org/10.1016/j.compscitech.2020.108048.

[17] S. Liparoti, V. Speranza, A. Sorrentino, G. Titomanlio, Mechanical properties distribution within polypropylene injection molded samples: effect of mold temperature under uneven thermal conditions, Polymers 9 (2017) 585, https://doi.org/10.3390/polym9110585.

[18] X. Wu, S. Shi, Z. Yu, T.P. Russell, D. Wang, AFM nanomechanical mapping and nanothermal analysis reveal enhanced crystallization at the surface of a semicrystalline polymer, Polymer 146 (2018) 188–195, https://doi.org/10.1016/j.polymer.2018.05.043.

[19] C. Vámos, L.J. Varga, B. Marosfői, T. Bárány, Role of extruded sheet morphology in phase separation and final morphology of superhydrophobic polypropylene, Period. Polytech. - Mech. Eng. 66 (2022) 260–271, https://doi.org/10.3311/PPme.20509.

[20] L.M. Vas, Z. Kocsis, T. Czigány, P. Tamás, G. Romhány, Novel evaluation method of acoustic emission data based on statistical fiber bundle cells, J. Compos. Mater. 53 (2019) 2429–2446, https://doi.org/10.1177/0021998319826666.

[21] L.M. Vas, Z. Rácz, Modeling and testing the fracture process of impregnated carbon-fiber roving specimens during bending: Part I, J. Compos. Mater. 38 (2004) 1757–1785.

[22] Á.D. Virág, L.M. Vas, P. Bakonyi, M. Halász, Analysing of the yarn pull-out process for the characterization of reinforcing woven fabrics, Fibers Polym. 20 (2019) 1975–1982, https://doi.org/10.1007/s12221-019-8978-9.

[23] L.M. Vas, P. Tamás, E. Bognár, P. Nagy, R. Késmárszky, K. Pap, G. Szebényi, Nonlinear fiber-bundle-cells-based phenomenological modeling of human tissue samples, Biomech. Model. Mechanobiol. 21 (2022) 1803–1823, https://doi.org/10.1007/s10237-022-01621-1.

[24] T. Tábi, T. Ageyeva, J.G. Kovács, Improving the ductility and heat deflection temperature of injection molded Poly(lactic acid) products: a comprehensive review, Polym. Test. 101 (2021), 107282, https://doi.org/10.1016/j.polymertesting.2021.107282.

[25] H. Chen, P. Cebe, Investigation of the rigid amorphous fraction in Nylon-6, J. Therm. Anal. Calorim. 89 (2007) 417–425, https://doi.org/10.1007/s10973-007-8215-4.

[26] S. Fehri, P. Cinelli, M. Coltelli, I. Anguillesi, A. Lazzeri, Thermal properties of plasticized poly (lactic acid) (PLA) containing nucleating agent, Int. J. Chem. Eng. Appl. 7 (2016) 85–88, https://doi.org/10.7763/IJCEA.2016.V7.548.

[27] M. Schneider, N. Fritzsche, A. Puciul-Malinowska, A. Baliś, A. Mostafa, I. Bald, S. Zapotoczny, A. Taubert, Surface etching of 3D printed poly(lactic acid) with NaOH: a systematic approach, Polymers 12 (2020), https://doi.org/10.3390/polym12081711.

[28] M. Hussain, A. Memic, N. Alothmany, R. Al-Dhaheri, F. Al-hazmi, H. Alhadrami, A. Khademhosseini, Characterization of fibrous scaffold using quantitative nano-mechanical mapping mode of atomic force microscope, J. Basic Appl. Biol. Int. 2 (2015) 2394–5820.

[29] S. Barrau, C. Vanmansart, M. Moreau, A. Addad, G. Stoclet, J.-M. Lefebvre, Crystallization behavior of carbon Nanotube−Polylactide nanocomposites, Macromolecules 44 (2011), https://doi.org/10.1021/ma200842n.

[30] J.W. Martin, Composite materials, in: Third Edition, in: J.W. Martin (Ed.), Materials For Engineering, Woodhead Publishing, 2006, pp. 185–215. https://doi.org/10.1533/9781845691608.2.185.